Check for updates

Effect of Bi-substitution into the A-site of multiferroic La₀.₈Ca₀.₂FeO₃ on structural, electrical and dielectric properties

H. Issaoui,[*ab] A. Benali,[bc] M. Bejar,[b] E. Dhahri,[b] B. F. O. Costa,[a] M. P. F. Graca[c] and M. A. Valente[c]

$(La_{0.8}Ca_{0.2})_{1-x}Bi_xFeO_3$ ($x = 0.00, 0.05, 0.10, 0.15$ and 0.20) (LCBFO) multiferroic compounds have been prepared by the sol−gel method and calcined at 800 °C. X-ray diffraction results have shown that all samples crystallise in the orthorhombic structure with the *Pnma* space group. Electrical and dielectric characterizations of the synthesized materials have been performed using complex impedance spectroscopy techniques in the frequency range from 100 Hz to 1 MHz and in a temperature range from 170 to 300 K. The ac-conductivity spectra have been analysed using Jonscher's power law $\sigma(\omega) = \sigma_{dc} + A\omega^s$, where the power law exponent (s) increases with the temperature. The imaginary part of the complex impedance (Z'') was found to be frequency dependent and shows relaxation peaks that move towards higher frequencies with the increase of the temperature. The relaxation activation energy deduced from the Z'' vs. frequency plots was similar to the conduction activation energy obtained from the conductivity. Hence, the relaxation process and the conduction mechanism may be attributed to the same type of charge carriers. The Nyquist plots (Z'' vs. Z') at different temperatures revealed the appearance of two semi-circular arcs corresponding to grain and grain boundary contributions.

1 Introduction

Perovskite-type ferrites with the general formula $AFeO_3$ are among the most promising materials in several fields of application. Recently, they have been used for fuel cells, sensors, magnetic memories, spintronic devices, *etc.*[1–5] In addition, great attention has been paid to the iron oxide $LaFeO_3$ (LFO) due to its excellent properties and use for technological applications, such as in transducers with magnetic modulation,[6] fuel cells,[7] catalysts,[8] chemical sensors,[9,10] magnetic materials[11,12] and oxygen permeation membranes.[13,14]

However, more recent studies have been conducted on doped iron oxides, such as $La_{1-x}Ca_xFeO_3$, due to their fascinating magnetic and electrical properties.[15,16] These compounds have a transition from ferromagnetic (FM) to paramagnetic (PM) state at $T_C = 670$ K.[17] The iron-based perovskite derivatives of general formula $La_{1-x}A_xFe_{1-y}B_yO_3$ (A = Ba, Ca, Pb, Sr,…/B = Cr, Sm, Nb,…) have been widely studied by combining the effects of substitution and of the preparation method to improve the dielectric, ferromagnetic and ferroelectric properties.[18–20]

ᵃCFisUC, Physics Department, University of Coimbra, P-3004-516 Coimbra, Portugal. E-mail: hajerissawui@yahoo.fr

ᵇLaboratoire de Physique Appliquée, Faculté des Sciences, Université de Sfax, B.P. 1171, 3000 Sfax, Tunisia

ᶜI3N and Physics Department, University of Aveiro, Aveiro, 3810-193, Portugal

In addition, these materials have a giant dielectric constant and a low dielectric loss around room temperature.[19] Materials with such properties have been used mainly in the manufacture of electronic devices, in particular such as capacitors and dynamic random access memories known as DRAM.[21]

Note here that the substitution of lanthanum ions by those of calcium has the effect of reducing electrical resistance and improving magnetic and dielectric properties, which allows the use of these materials $La_{1-x}Ca_xFeO_3$ (LCFO) as gas sensors and as a cathode in solid oxide fuel cells (SOFC).[22–25]

In our previous study, we have proved that the relaxation process in $La_{0.8}Ca_{0.2}FeO_3$ compound prepared is of polaronic type, which is caused by the jumps of the charge carriers between the different iron ions.[26] The NSPT model (small polaron without overlapping tunnel effect) has been used to study the conduction mechanism of the $La_{0.8}Ca_{0.2}FeO_3$ compound. We also confirmed a huge dielectric constant with low dielectric loss tangent for the $(La_{0.8}Ca_{0.2})_{0.9}Bi_{0.1}FeO_3$ compound.[27] This later also presented two relaxation processes, which are associated to grains and boundary grains contributions. This compound has been annealed at 800 °C as the series of samples we present in the present study.

In previous works we studied several properties of the $(La_{0.8}Ca_{0.2})_{1-x}Bi_xFeO_3$ ($x \leq 0.20$) series annealed at different temperatures.[28,29] We chose to do a more detailed study, namely on electrical and dielectrical properties, on the series annealed

at 800 °C as the grain size of the samples is smaller in this series.

In this study, we focus on the synthesis and study of the effect of insertion bismuth ions in A-site of $(La_{0.8}Ca_{0.2})_{1-x}Bi_x$-$FeO_3$ (with x = 0.00, 0.05, 0.10, 0.15 and 0.20).

2 Experimental techniques

The nanosized crystalline $(La_{0.8}Ca_{0.2})_{1-x}Bi_xFeO_3$ (x = 0.00, 0.05, 0.10, 0.15 and 0.20) LCBFO compounds have been prepared by the sol–gel method[30] using as raw precursors lanthanum nitrate, bismuth nitrate, calcium nitrate, ferric nitrate and citrate acid (all analytically pure).

$$0.8(1-x)La(NO_3)_3 + 0.2(1-x)Ca(NO_3)_2 + xBi(NO_3)_2 + Fe(NO_3)_3 \rightarrow (La_{0.8}Ca_{0.2})_{1-x}Bi_xFeO_3$$
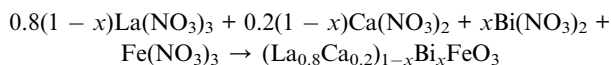
First, the precursors were mixed in distilled water. Afterwards, citric acid and ethylene glycol were added with constant stirring at room temperature for 5 h, in order to improve the consistency and the consequent formation of the gel. The mixture obtained was then heated to 170 °C until the formation of a black powder. This powder was pressed into thin pellets about 12 mm in diameter and *ca.* 1.5 mm thick and subjected to heat treatments at different temperatures (400 and 600 °C for 12 hours, 700 °C for 24 hours), interrupted by grinding cycles. Finally, the powders obtained were calcined at 800 °C (LCBFO800) for 72 hours.[30] The phase purity, homogeneity, lattice structure and cell parameters of the synthesized compounds have been checked out by X-ray diffraction (XRD) analysis, using a Bruker 8D Advance X-ray powder diffractometer, with Cu Kα_1 radiation (λ = 1.5406 Å), in θ–2θ Bragg–Brentano geometry. The acquisition has been chosen to be in the 2θ range of 5–100°, with a step of 0.02° and an acquisition time for each step of 1 s. The XRD data have been also used to obtain the lattice parameters by means of Rietveld analysis,[31] using the FullProf program.

For the electrical measurements, a system formed by a vertical electric furnace and a dry rotary pump, in a closed cycle setup, connected to the extremes of the furnace has been used. This non-inductive electrical furnace operates from room temperature up to 1473 K. In each measurement, the sample has been mechanically pressed between two parallel platinum plates, forming the electrodes. The ac impedance of the samples has been measured between 170 and 300 K, and in the frequency range of 100 Hz up to 1 MHz, using an Agilent 4294A Precision Impedance Analyzer.

3 Results and discussion

3.1 Structural properties

3.1.1 X-ray diffraction. The room temperature X-ray diffraction patterns, for the studied LCBFO compounds (Fig. 1(a)), show that these compounds exhibit a perovskite phase as a large major phase[28,29] so the samples are considered as single phased.

3.1.2 Refinement by the Rietveld method. The performed Rietveld refinements of the XRD data, undertaken using the FullProf program, reveal that the studied compounds crystallize in an orthorhombic structure with *Pnma* space group. The refinement results are shown in Fig. 1(b) and the structure parameters are summarized in Table 1, from which we can note that the insertion of bismuth leads to an increase in the volume. We also notice a variation of the angle Fe–O–Fe and the distance Fe–O that can be explained by the effect of the difference in the size of the cations occupying site A. Indeed, the ionic radius of bismuth ($r_{Bi^{3+}}$ = 1.03 Å) is smaller than that of calcium ($r_{Ca^{2+}}$ = 1.18 Å) and lanthanum $r_{La^{3+}}$ = 1.216 Å.[30] The crystal structure of LCBFO compounds illustrating the bonds as well as the FeO$_6$ octahedra after refinement is introduced in the inset of Fig. 1(a).

In order to confirm the structure of materials, Goldschmidt has defined a tolerance factor t_G which provides information on
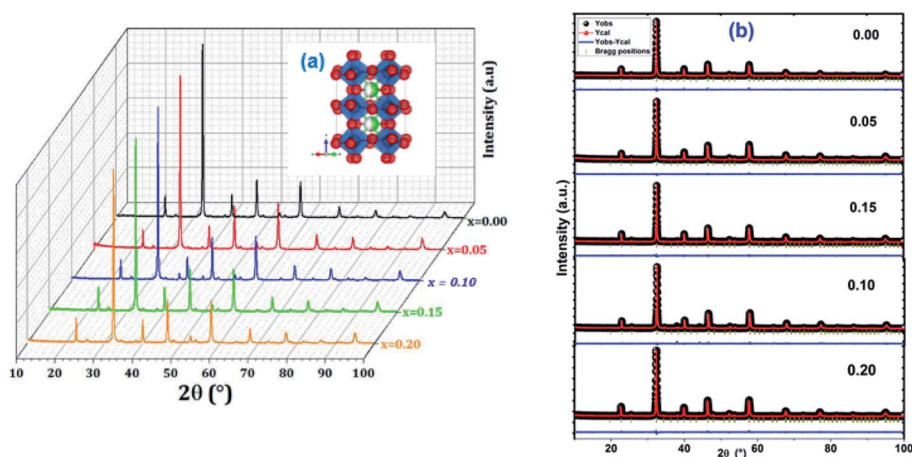

Fig. 1 (a) Room temperature XRD patterns for $(La_{0.8}Ca_{0.2})_{1-x}Bi_xFeO_3$ (x = 0.00, 0.05, 0.10, 0.15 and 0.20) compounds. (b) The FullProf refined XRD; observed (red circle), calculated (black continuous line) and difference patterns (blue line) of X-ray diffraction data. The vertical tick indicates the Bragg positions. The inset exhibits the crystal structure.

Table 1 Lattice parameters (a, b, c, V) obtained from the refinement of the XRD data for $(La_{0.8}Ca_{0.2})_{1-x}Bi_xFeO_3$ (x = 0.00, 0.05, 0.10, 0.15 and 0.20) compounds

x	0.00	0.05	0.10	0.15	0.20
Space group	Pnma				
$\langle r_A \rangle$ (Å)	1.208	1.199	1.190	1.181	1.173
Tolerance factors (t)	0.912	0.909	0.905	0.902	0.899
a (Å)	5.524	5.526	5.528	5.533	5.539
b (Å)	7.808	7.809	7.812	7.813	7.822
c (Å)	5.527	5.525	5.528	5.526	5.530
Unit cell volume V (Å^3)	59.609	59.607	59.695	59.734	59.907
Fe–O$_1$	1.991	1.987	1.964	1.988	1.990
Fe–O$_2$	2.013	2.002	2.111	1.997	1.999
Fe–O$_2$	1.972	1.982	1.940	1.985	1.9870
$\langle$Fe–O$\rangle$	1.992	1.990	2.005	1.990	1.992
Fe–O$_1$–Fe	157.420	158.430	159.748	158.571	158.576
Fe–O$_2$–Fe	158.210	158.190	151.611	158.174	158.174
$\langle$Fe–O–Fe$\rangle$	157.815	158.310	155.679	158.372	158.375
χ^2	1.251	1.280	2.435	1.245	1.264
R_p	10.8	10.2	14.5	15.5	12.0
R_{wp}	12.2	10.7	15.8	16.5	11.8
R_e	10.9	9.43	10.1	14.8	10.5

the stability and distortion of the crystal structure using geometric criteria:[32]

$$t_G = \frac{r_A + r_O}{(r_B + r_O)\sqrt{2}}$$

where r_A, r_B and r_O are the radii of A, B and O site ions in the ABO$_3$ structure, respectively.

The arithmetic values of the ionic rays of ions occupying sites A, B and O respectively are calculated as follows:

$$\langle r_O \rangle = r_{O^{2-}}$$

$$\langle r_B \rangle = r_{Fe^{3+}}$$

$$\langle r_A \rangle = 0.8(1 - x)r_{La^{3+}} + 0.2(1 - x)r_{Ca^{2+}} + xr_{Bi^{3+}}$$

The calculated tolerance factor values are grouped in the Table 1. According to this table, it can be seen that the t_G values decrease with the increase of bismuth rate due to a decrease in the average ionic radius of the site A. The decrease in the tolerance factor t_G bring about the system to the most symmetrical structure. Based on the Tokura et al. study,[33] we can deduce that our LCBFO compounds show an orthorhombic agreement.

3.1.3 Debye Scherrer and Williamson–Hall method. In order to determine the average crystallite size, we have used the Scherer and the Williamson–Hall methods. For both methods, the average crystallite size is obtained from the XRD peaks, and below is a detailed explanation of these two methods of calculation.

Concerning the method of Debye–Scherer,[34] the expressed as follows:

$$D_{SC} = \frac{0.9 \times \lambda}{\beta \times \cos\theta} \qquad (1)$$

with λ the used wavelength, θ the Bragg angle for the most intense peak and β the half height width of this peak.

For the Williamson–Hall method, the widening of the X-ray line (β) equal to the expansion caused by the deformation of the lattice (β_{strain}) present in the material[35] plus the contribution of crystallite size (β_{size}).

$$\beta = \beta_{strain} + \beta_{size} \qquad (2)$$
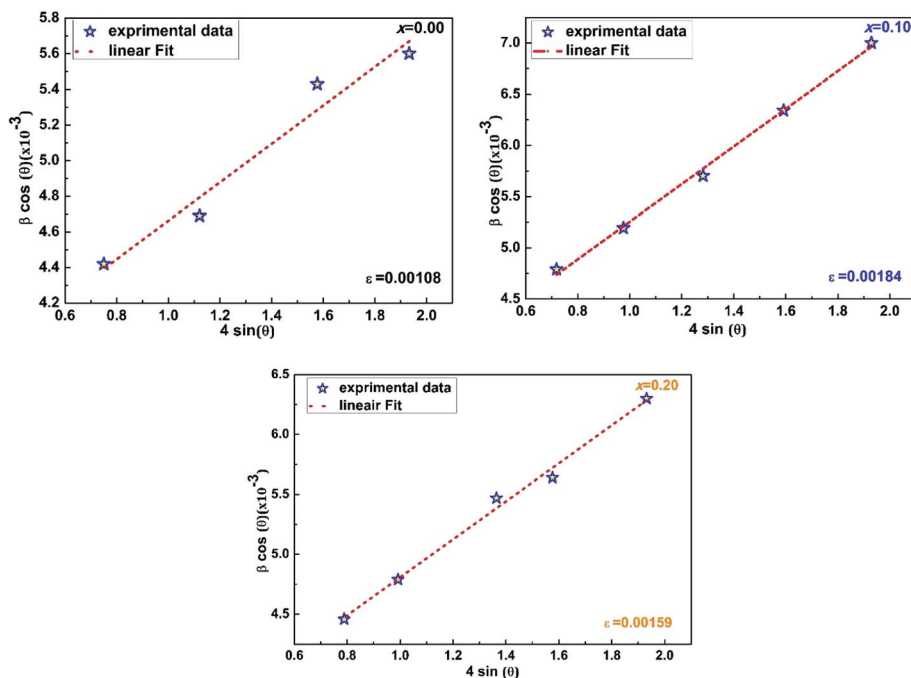
Fig. 2 Williamson–Hall plot of $(La_{0.8}Ca_{0.2})_{1-x}Bi_xFeO_3$ (x = 0.00, 0.10, and 0.20) compounds.

Paper

Table 2 The average sizes of the crystallites obtained by the formula of Scherrer (D_{SC}) and by the formula of Williamson–Hall (D_{WH}) for $(La_{0.8}Ca_{0.2})_{1-x}Bi_xFeO_3$ (x = 0.00, 0.05, 0.10, 0.15 and 0.20) compounds

x	0.00	0.05	0.10	0.15	0.20
D_{SC} (nm)	33.60	34.64	36.47	37.42	37.61
D_{WH} (nm)	38.82	40.06	41.05	42.56	43.07
ε (%)	0.108	0.125	0.184	0.149	0.159

Table 3 The values of the apparent density (d_B), the X-ray density (d_x) and the porosity (p) for $(La_{0.8}Ca_{0.2})_{1-x}Bi_xFeO_3$ (x = 0.00, 0.05, 0.10, 0.15 and 0.20) compounds

x	0.00	0.05	0.10	0.15	0.20
d_B (g cm^{-3})	3.343				
d_x (g cm^{-3})	6.218	6.357	6.483	6.627	6.755
p (%)	46.226	47.404	48.444	49.547	50.500
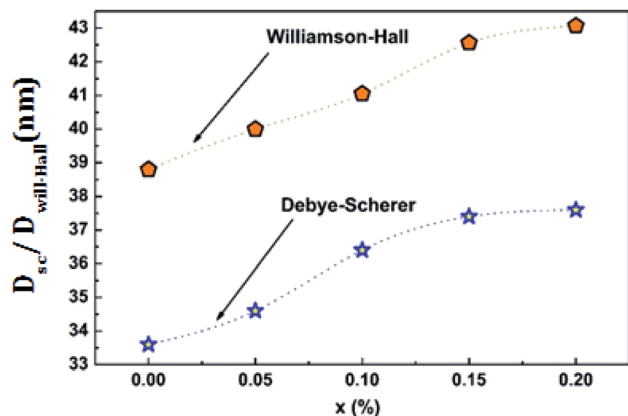
Fig. 3 Variation of the average size for the crystallites as a function of the bismuth rate calculated by the two methods of Debye–Scherer and Williamson–Hall for $(La_{0.8}Ca_{0.2})_{1-x}Bi_xFeO_3$ (x = 0.00, 0.05, 0.10, 0.15 and 0.20) compounds.

where $\beta_{strain} = 4\varepsilon \tan \theta$: with ε is a coefficient related to strain effect on the crystallites and $\beta_{size} = \dfrac{k\lambda}{D \cos \theta}$: from Scherer's formula $\beta = \dfrac{k \times \lambda}{D \cos \theta} + 4\varepsilon \tan \theta$.

Therefore, (eqn (2)) becomes: $\beta \cos \theta = \dfrac{k\lambda}{D} + 4\varepsilon \sin \theta$.

Afterwards, by the representation of $\beta \cos \theta = f(4 \sin \theta)$ (Fig. 2), we can determine the crystallite size D_{WH} and the microstrain, respectively, from the intercept of the line at x = 0 and from the slope of the linearly fitted data. The obtained values for the crystallite sizes D_{SC} and D_{WH} and for the microstrain ε are summarized in Table 2.

Fig. 3 shows the variation of the average size of the crystallites as a function of the bismuth level calculated by the two methods for the LCBFO compounds.

From Table 2 and Fig. 3, we can confirm the nanometric size of the crystallites. It is worth noting that the crystallite size calculated by Debye–Scherrer technique is slightly lower than that calculated by Williamson–Hall method because the broadening effect due to the microstrains completely excluded in Debye–Scherrer technique.

Also, we note a small increase in the size of the crystallites by increasing the bismuth rate. This increase is proportional previously detected for the volume.

3.1.4 Porosity. The porosity p of our compounds was calculated using the following relationship:[36]

$$p(\%) = \left(1 - \frac{d_B}{d_x}\right) \times 100 \qquad (3)$$

where: d_x is the X-ray density:

$$d_x = \frac{M}{\mathcal{N} \times V} \qquad (4)$$

and d_B the apparent density:

$$d_B = \frac{m_P}{V_P} \qquad (5)$$

with M is the molecular mass, $\mathcal{N}$ is the Avogadro number, V the volume determined from the XR results, m_P is the mass of the pellet and V_P is the volume of the pellet.

The values of the density of XR (d_x), the apparent density (d_B) and the porosity (p) are summarized in the Table 3. According to this table, we note an increase in the porosity with the increase in the rate of bismuth. On the other hand, our (p) values are found to be very similar to those mentioned by N. Rezlescu et al.[37] and Q. Rong et al.[38] for such an application (gas sensors).

3.2 Morphological study

3.2.1 Scanning electron microscope (SEM). Scanning electron microscopy (SEM) images of the LCBFO compounds are displayed in Fig. 4. These images show a relatively uniform grain size distribution, indicating that the sol–gel method is a good process to prepare uniform and dense powders. The micrographs of the samples with x > 0.00 (x = 0.05, 0.10, 0.15 and 0.20) present an important homogeneity in the microstructure with an increase of the grain size. This put forward to consider that compounds containing Bi exhibit a higher fraction of larger crystalline grains.

3.2.2 Energy dispersive X-ray spectroscopy, EDS analysis. The elemental composition of our compounds has been studied by an analysis system (EDS) (Fig. 5). We can note the presence of all the chemical elements (La, Ca, Fe, O and Bi) initially introduced during the preparation, which indicates that all the elements are non-volatile at 800 °C.

The elementary compositions in terms of atomic percentages and percentages by weight are shown in the Table 4. These values are almost in agreement with the stoichiometry of the starting materials used for the preparation of samples.

4 Dielectric and electrical studies

4.1 Complex impedance spectrum

4.1.1 Variation of the real part of impedance Z'. Fig. 6 shows the variation of the real part of the impedance (Z') as a function of the frequency at different temperatures for all the LCBFO compounds. We can note that, at low frequency and temperature ranges, the Z' values are high which decrease with
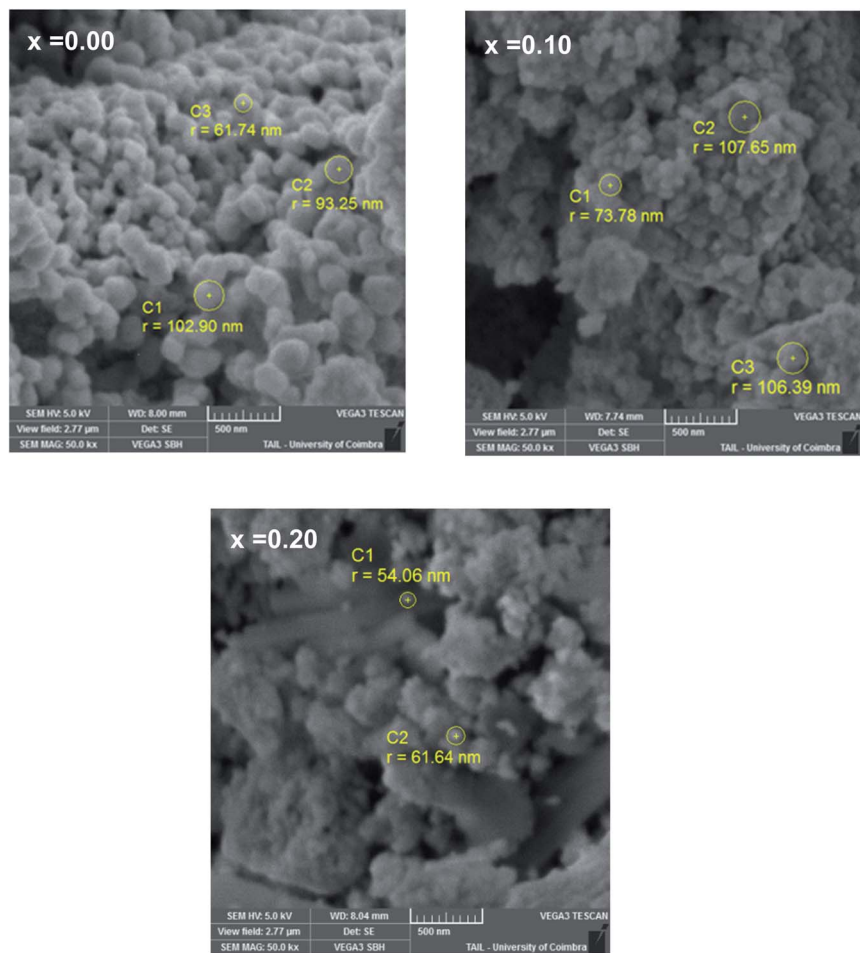
Fig. 4 SEM micrographs of $(La_{0.8}Ca_{0.2})_{1-x}Bi_xFeO_3$ (x = 0.00, 0.10, and 0.20) compounds.
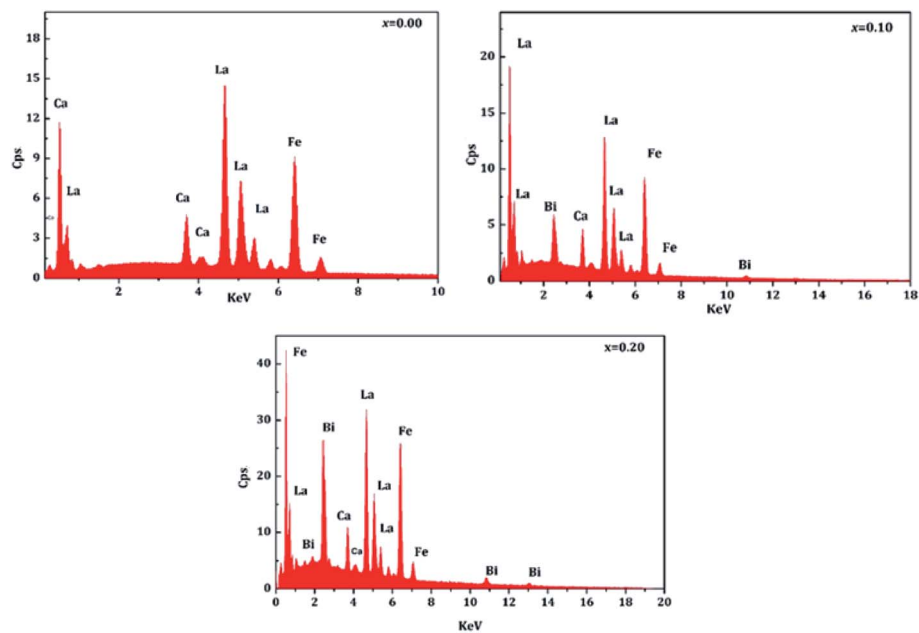
Fig. 5 EDS spectra of $(La_{0.8}Ca_{0.2})_{1-x}Bi_xFeO_3$ (x = 0.00, 0.10 and 0.20) compounds.

Table 4 Elemental compositions in terms of atomic percentages and weight percentages for $(La_{0.8}Ca_{0.2})_{1-x}Bi_xFeO_3$ ($x = 0.00$, 0.05, 0.10, 0.15 and 0.20) compounds

Element	Weight (%)	Atomic (%)
$x = 0.00$		
Oxygen	22.5 (7.4)	58.1
Calcium	3.7 (0.4)	4.3
Iron	25.6 (2.0)	20.9
Lanthanum	48.2 (3.7)	16.7
$x = 0.05$		
Oxygen	29.7 (9.1)	69.6
Calcium	3.3 (0.4)	3.2
Iron	23.1 (1.7)	15.6
Lanthanum	40.8 (3.1)	11.0
Bismuth	3.1 (0.5)	0.6
$x = 0.10$		
Oxygen	23.4 (8.3)	71.6
Calcium	3.5 (0.4)	2.8
Iron	24.3 (1.9)	14.7
Lanthanum	41.2 (3.4)	9.7
Bismuth	7.7 (0.8)	1.2
$x = 0.15$		
Oxygen	25.5 (7.5)	66.1
Calcium	3.0 (0.3)	3.1
Iron	23.8 (1.7)	17.7
Lanthanum	36.6 (2.6)	11.0
Bismuth	11.1 (1.1)	2.2
$x = 0.20$		
Oxygen	24.7 (7.9)	65.0
Calcium	3.1 (0.3)	3.3
Iron	23.5 (1.7)	18.1
Lanthanum	34.5 (2.5)	10.7
Bismuth	14.2 (1.3)	2.9

the increase of the temperature putting in evidence of a negative thermal coefficient of resistance (NTCR) and proves the improvement in the dc-conductivity σ_{dc}[39] as result of the increase in the mobility of charge carriers.[40] The same phenomenon has already been observed in many other materials of the perovskite type.[41] In addition, towards the high frequencies, we note that the impedance spectra merge and show an independent variation of the temperature. The Z' behaviour of our compounds at low and high frequencies is in perfect agreement with the results reported in the literature.[42] In the intermediate frequency region, a gradual decrease in Z' with increasing frequency and temperature was observed for all compounds which is a sign of the great charge carriers mobility, indicating a reinforcement of the electrical conductivity by increasing the temperature and the frequency.[43] We also note that for the compounds with $x > 0.10$, and in the region of the intermediate frequencies, Z' presents a small plateau, then decreases thereafter until the fusion towards the high frequencies. This may be due to the existence of two different contributions, which will be detailed in the following.

4.1.2 Variation of the imaginary part of impedance Z''. The variation of the imaginary part of the impedance (Z'') for the LCBFO compounds as a function of the frequency at different temperatures is shown in Fig. 7. It is clear that, for all the compounds, the increase in the frequency is accompanied by a rise in the values of the imaginary part of the impedance (Z'') until reaching a maximum value at a particular frequency and then decreases with increasing frequency. This proves the existence of a relaxation phenomenon within our materials. Note also that for compounds with a bismuth rate greater than 10%, the curves of Z'' as a function of frequency clearly show the existence of two peaks. The peaks at low frequencies are attributed to the grain boundaries while those at high frequencies are the characteristic of the grains contribution.

In addition, for all compounds, the relaxation peaks move towards the high frequencies when we increase the temperature, which indicates that the relaxations are thermally activated.[44]

Using the frequency positions of these peaks (f_{max}), we have calculated the activation energies for the two contributions. The logarithmic variations of the frequencies corresponding to the relaxations $\ln(f_{max})$ as a function of the temperature inverse ($1/T$) of the LCBFO compounds are shown in Fig. 8. We note that, for all the compounds and for the both contributions, this variation leads to linear behaviour with a slope, which varies according to the rate of substitution. This means that the relaxations perfectly follow the Arrhenius law given by the following equation:

$$f_{max} = f_0 \exp\left(-\frac{E_a}{k_B T}\right) \tag{6}$$

with f_0 represents a pre-exponential factor, E_a is the activation energy and k_B is the Boltzmann constant.

From the activation energy values (Fig. 8), we can note that the activation energy relative to the relaxation of the grains shows an increasing tendency with substitution and that it reaches a maximum value for the compound with 10% of bismuth then decreases for further bismuth concentrations. This decrease may be due to the increase in the charge carriers during the increase in the Bi-content.

According to literature, when the relaxation activation energy of such material is in the range between 0.2 and 0.4 eV, the relaxation process is known to be polaronic with a jump between B-site ions states.[45,46] Accordingly, we deduce that the polaronic nature of the relaxation processes in the studied compounds.

4.1.3 Analysis of the Nyquist spectra. The Nyquist diagram is one of the most used graphical representations in impedance spectroscopy which consists in plotting the imaginary part of the measured impedance (Z'') as a function of the real one (Z') in a coordinate system orthonormal Cartesian. This diagram generally gives a succession of arcs of circle, each of which is associated with one of the contributions (grains, grains boundaries, electrodes, etc.) that constitute the studied material.[47]

The Nyquist diagrams relating to our LCBFO compounds, which are obtained at different temperatures, are shown in
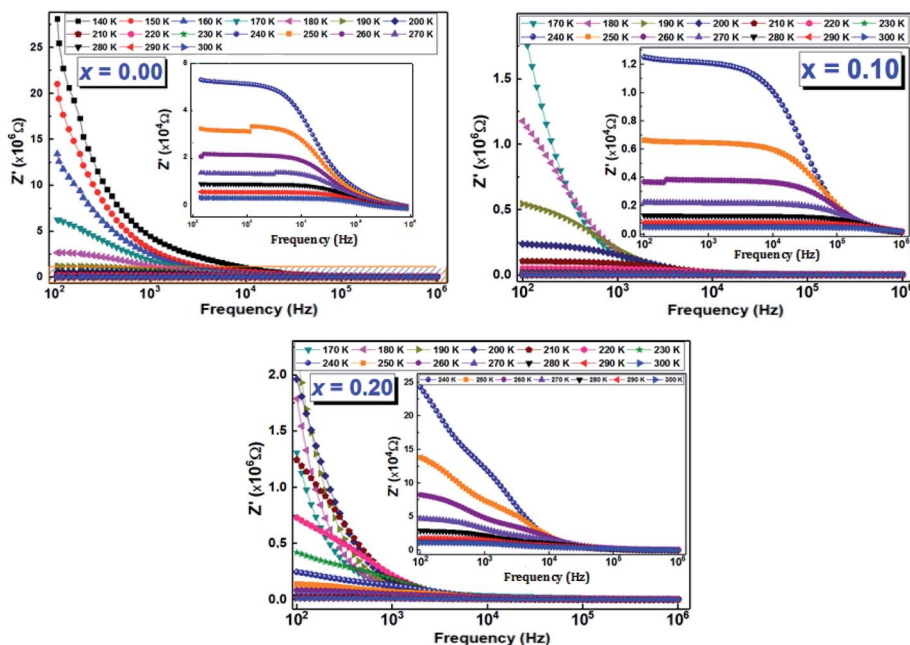
Fig. 6 The frequency dependence of the real part of the complex electrical impedance (Z') at several temperatures of $(La_{0.8}Ca_{0.2})_{1-x}Bi_xFeO_3$ (x = 0.00, 0.10, and 0.20) compounds.

Fig. 9. All diagrams are made up of two arcs of circles located below the real axis; the first one is observed at high frequencies while the second arc of circle, having a larger radius, is observed at low frequencies. This second arc is associated to the grain boundaries resistance (R_{GB}) contribution, while the first one represents the grains contribution.[48] We also note that, for all LCBFO compounds, the radii of the half-arcs decrease while

increasing the temperature, which proves the increase in electrical conductivity with temperature.[49]

Given the existence of two arcs, the adjustment of Nyquist diagrams must be done with an equivalent circuit containing two sub-circuits connected in series.

We performed the modeling with Z-View software,[50] and the best fit is obtained using an equivalent electrical circuit
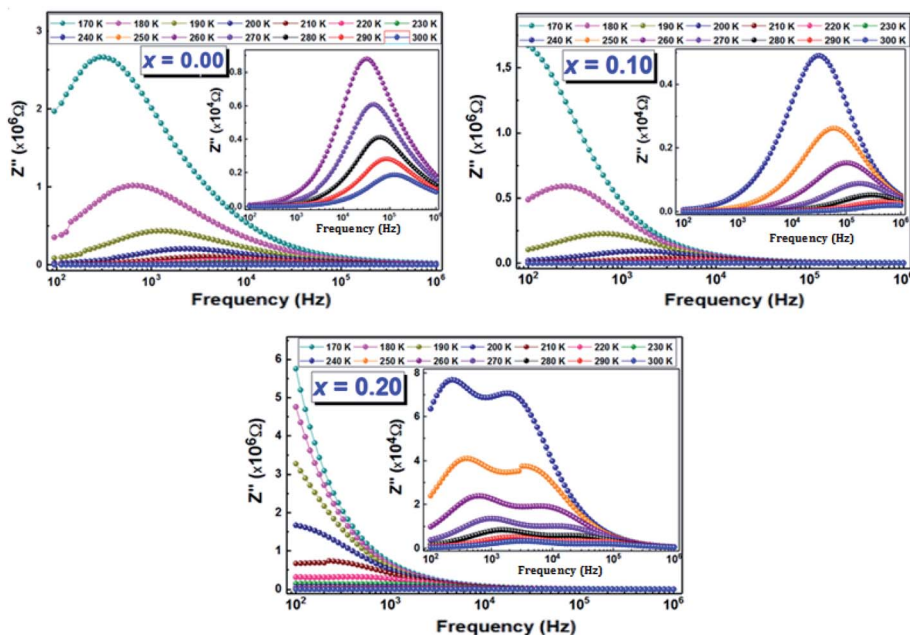

Fig. 7 The frequency dependence of the imaginary part of the complex electrical impedance (Z'') at several temperatures of $(La_{0.8}Ca_{0.2})_{1-x}Bi_xFeO_3$ (x = 0.00, 0.10, and 0.20) compounds.
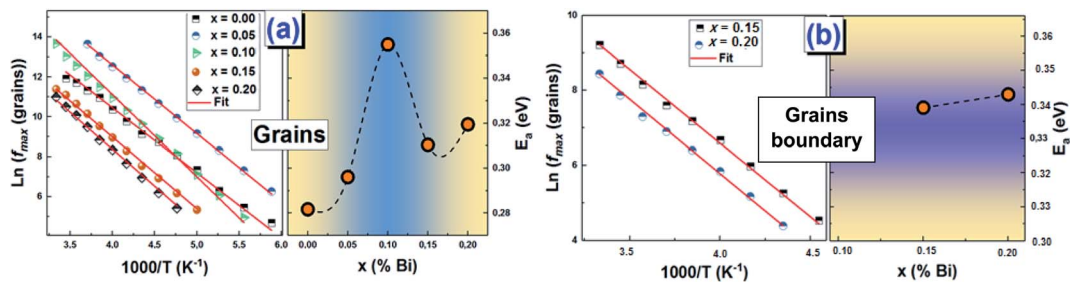
Fig. 8 Variation of $\ln(f_{max}(Z''))$ as a function of $1000/T$ and the activation energies corresponding to (a) gains and (b) grain boundaries of $(La_{0.8}Ca_{0.2})_{1-x}Bi_xFeO_3$ ($x = 0.00$, 0.05, 0.10, 0.15 and 0.20) compounds.
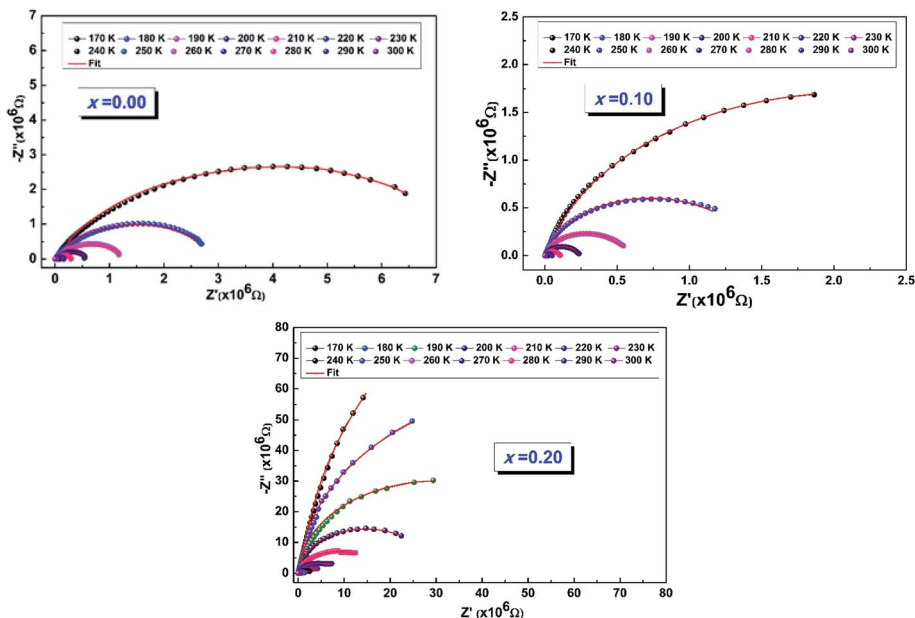

Fig. 9 The fit of the experimental data using this equivalent circuit of Fig. 10.

consisting of a series combination of two contributions. The first contribution corresponds to grain boundaries (R_{GB}–CPE_{GB}) (with CPE is the fractal impedance capacity) and the second is associated with grains (R_G–C_G), as shown in Fig. 10.

The resistance and capacitance values of the two contributions, for all the compounds, resulting from the adjustment with the Z-View software using the circuit mentioned above, are tabulated in Table 5. We note, from this table, that the

Fig. 10 The equivalent circuit formed by a parallel combination of grain resistance. (R_G–C_G circuit) and constant phase element impedance (ZCPE) (R_{GB}–CPE_{GB} circuit).

resistance of the two contributions decreases with temperature, which confirms the semiconductor behaviour of all the LCBFO compounds.[51] On the other hand, we can clearly see that for all compounds, the resistance of grain boundaries (R_{GB}) is greater than that of grains (R_G). This can be attributed to the fact that the atomic arrangement near the region of the grain boundaries is disordered, resulting in increased electron scattering. The logarithmic variations of the resistances R_G and R_{GB} as a function of the temperature inverse for our compounds are illustrated in Fig. 11(a) and (b). The activation energies are determined from Arrhenius' law:

$$R_{G/GB} = R_0 \exp\left(\frac{E_a}{k_B T}\right) \quad (7)$$

The activation energy values E_a of the two contributions are collated in Table 6. We note that the E_a values of grain boundaries are slightly higher than those of grains, which indicates a higher resistive behaviour than that of grains.
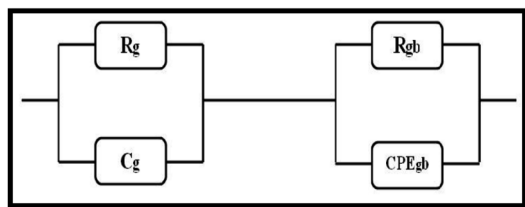
Table 5 Electrical parameters of equivalent circuit of $(La_{0.8}Ca_{0.2})_{1-x}Bi_xFeO_3$ (x = 0.00, 0.10 and 0.20) compounds at several temperatures

T (K)	R_{JG} ($\times 10^5\ \Omega$)	CPE_{JG} ($\times 10^{-9}$ F)	α	R_G ($\times 10^3\ \Omega$)	C_G ($\times 10^{-10}$ F)
$x = 0.00$					
170	76.60	0.43	0.75	1.85	0.24
180	37.65	0.64	0.74	1.32	3.90
190	21.28	1.06	0.73	0.84	3.70
200	9.86	1.31	0.76	0.51	2.50
210	5.30	1.71	0.74	0.31	2.18
220	3.30	2.13	0.75	0.21	1.90
230	2.01	2.36	0.76	0.15	1.67
240	1.19	2.30	0.78	0.10	1.50
250	0.67	1.62	0.82	0.07	1.24
260	0.43	1.89	0.82	0.06	1.37
270	0.26	1.25	0.87	0.04	1.28
280	0.18	1.62	0.86	0.04	1.43
290	0.12	1.57	0.87	0.03	1.50
300	0.08	1.51	0.77	0.02	2.02

T (K)	R_{GB} ($\times 10^4\ \Omega$)	CPE_{GB} ($\times 10^{-9}$ F)	α	R_G ($\times 10^3\ \Omega$)	C_G ($\times 10^{-10}$ F)
$x = 0.10$					
170	1189.69	1.04	0.86	7.86	0.20
180	5440.79	1.06	0.87	4.18	0.30
190	3215.82	1.10	0.88	2.65	0.38
200	1564.07	1.18	0.88	1.68	0.39
210	845.46	1.50	0.69	1.10	53
220	524.89	9.50	0.78	0.72	73
230	335.53	4.35	0.83	0.54	10.62
240	198.32	3.40	0.85	0.38	13.20
250	111.15	1.70	0.89	0.28	22
260	71.05	2.93	0.86	0.22	22.9
270	47.89	5.46	0.83	0.16	16.33
280	35.90	9.17	0.8	0.12	15
290	22.95	22.20	0.75	0.09	12.31
300	15.47	13.76	0.54	0.086	9.76
$x = 0.20$					
170	221	22.10	0.40	13.80	0.24
180	122.91	72.92	0.36	8.15	0.26
190	82.71	10.90	0.38	4.73	0.27
200	53.36	48.61	0.47	3.00	0.30
210	30.86	9.19	0.88	2.04	1.09
220	18.65	8.92	0.90	1.46	4.90
230	11.53	9.02	0.91	1.06	5.39
240	6.51	9.59	0.93	0.79	5.85
250	3.53	1.02	0.90	0.58	6.50
260	2.13	1.19	0.94	0.46	6.48
270	1.50	1.40	0.89	0.32	6.87
280	1.05	1.65	0.88	0.24	7.26
290	0.66	2.00	0.87	0.19	7.69
300	0.50	1.98	0.978	0.14	5.87

4.2 Dielectric relaxation study

4.2.1 Analysis of the complex modulus. Fig. 12 shows the evolution of relaxation peaks with frequency and temperature.

For the $La_{0.8}Ca_{0.2}FeO_3$ ($x = 0.00$) compound, the frequency variation of the imaginary part of the modulus presents a single clear relaxation (peak) in the frequency range $f > 5$ kHz. This compound shows also very broadening peaks at lower frequencies which their maximums were not detectable. However, the insertion of bismuth into A-site ($x \neq 0.00$) induces

a change in the trend of the dielectric relaxation process; this peak was clearly registered at lower frequencies and for all temperatures, which is ascribed to the grains contribution. While the second one detected at high frequencies, is attributed to grain boundaries. We also notice that all the peaks move towards the high frequencies when increasing the temperature. This displacement can be linked to the activated thermal energy of the charge carriers in the material, which increases with temperature. In addition, we note that, for a given temperature,
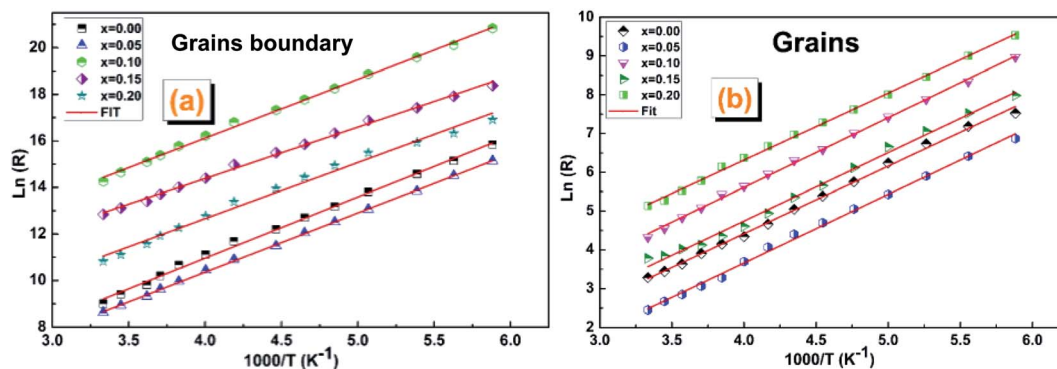
Fig. 11 The Arrhenius plots ($\ln(R)$ *vs.* $(1000/T)$) corresponding to (a) grain boundaries and (b) gains of $(La_{0.8}Ca_{0.2})_{1-x}Bi_xFeO_3$ ($x = 0.00$, 0.05, 0.10, 0.15 and 0.20) compounds.

Table 6 Activation energies values of $(La_{0.8}Ca_{0.2})_{1-x}Bi_xFeO_3$ ($x = 0.00$, 0.05, 0.10, 0.15 and 0.20) compounds

x	0.00	0.05	0.10	0.15	0.20
E_a of grains (eV)	0.1500	0.1525	0.1548	0.1521	0.1489
E_a of grains boundary (eV)	0.2267	0.2199	0.2175	0.1978	0.2079

the width of the peaks increases with the increase in the bismuth rate and especially for the peaks relating to grain boundary contribution. This may be due to the diffusive movement of the charge carriers and/or the presence of non-uniformities.[52]

The activation energies (E_a) for both contributions (grains and grain boundaries) were determined using the maximum frequency (f_{max}) for each temperature and based on the Arrhenius law (eqn (6)):

We present the adjustment results and the activation energy values E_a of the two contributions of all the LCBFO compounds in both Fig. 13(a) and (b).

We find that all the determined E_a values are in good agreement with those previously deduced from the study of the imaginary part of the impedance Z''. Again, and according to the activation energy values, we confirm the polaronic-type relaxation processes in the studied LCBFO compounds.

4.2.2.   Analysis of the angle of the dielectric loss tg(δ). For all LCBFO compounds, the evolution of the angle of the dielectric loss known as tg(δ) as a function of temperature and frequency is shown in Fig. 14. Firstly, we can notice that the angle of the dielectric loss, in the range of the high temperatures and low frequencies, increases with bismuth concentration lower or equal to 10%, to decrease considerably for higher rates. This proves the usefulness of the bismuth insertion,
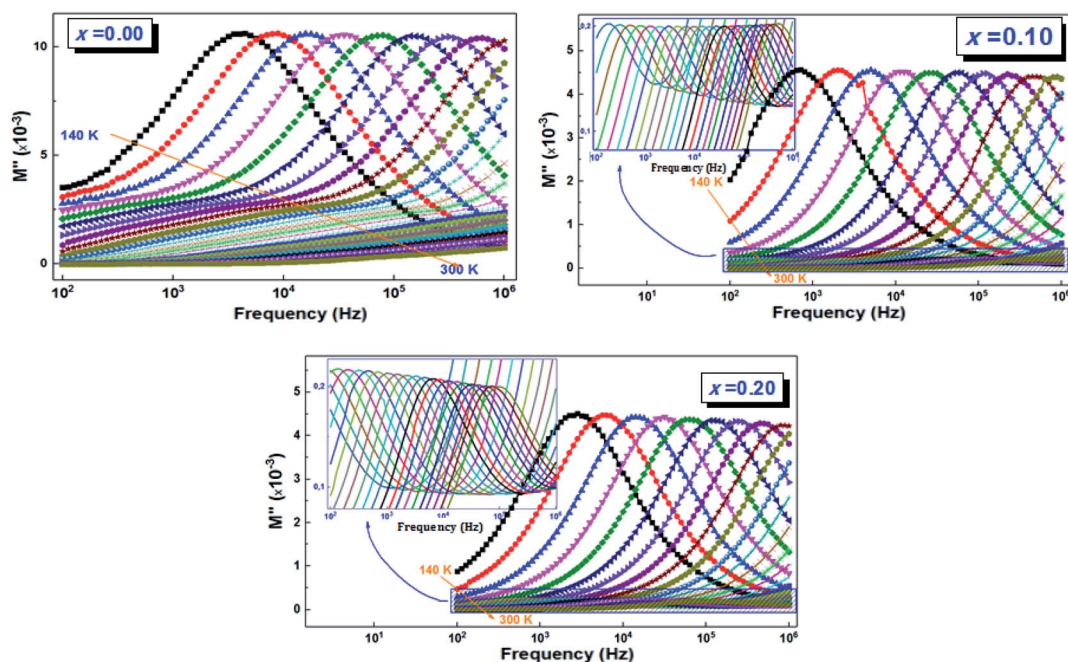

Fig. 12 Variation of the imaginary part of the electric modulus (M'') as a function of frequency and temperature of $(La_{0.8}Ca_{0.2})_{1-x}Bi_xFeO_3$ ($x = 0.00$, 0.10, and 0.20) compounds.
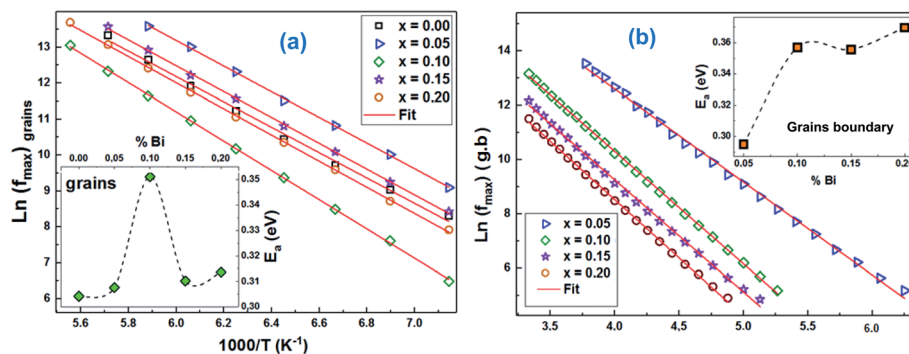
Fig. 13 Variation of $\ln(f_{max}(M''))$ as a function of $1000/T$ and the activation energies corresponding to (a) gains and (b) at grain boundaries of $(La_{0.8}Ca_{0.2})_{1-x}Bi_xFeO_3$ (x = 0.00, 0.05, 0.10, 0.15 and 0.20) compounds.
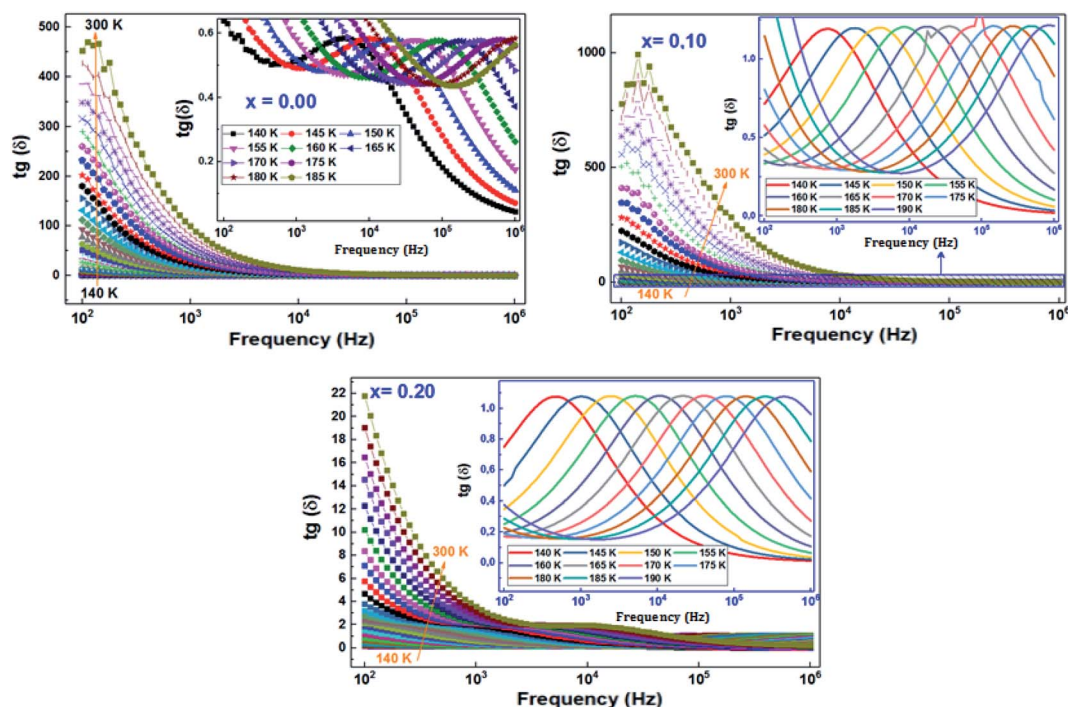

Fig. 14 Variation of loss tangent (tan δ) as a function of frequency at different temperatures of $(La_{0.8}Ca_{0.2})_{1-x}Bi_xFeO_3$ (x = 0.00, 0.10, and 0.20) compounds.

which has the consequence of reducing the dielectric tangent loss. The fact that this parameter represents the ratio of imaginary part to the real part of the complex permittivity, we can conclude consequently that, the lower tg(δ), the greater the dielectric constant, which results in more storage of the applied electrical energy with at least a small loss in the form of thermal energy.

On the other hand, for all compounds, the dielectric tangent loss shows maximum peaks which are found to move towards higher frequency range when increasing temperature, which confirms the thermally activated nature of the relaxation processes.

In order to calculate the activation energies with the Arrhenius relationship, we have determined the maximum frequency corresponding to the relaxation peaks. The tracing of the logarithmic variation of these frequencies as a function of the temperature inverse (Fig. 15) reveals the presence of straight lines whose slopes allowed us to go back to the activation energy (the inset of Fig. 15). It turns out that the variation of this activation energy as a function of the substitution rate is identical to those previously deduced from Z'' and from modulus M'', which proves that the relaxations in our compounds are attributed to the same process.

5 Conductivity study

The variation of the product of conductivity and temperature ($\sigma_{ac} \times T$) as a function of the inverse of the temperature ($1000/T$), recorded at different frequencies of all the LCBFO
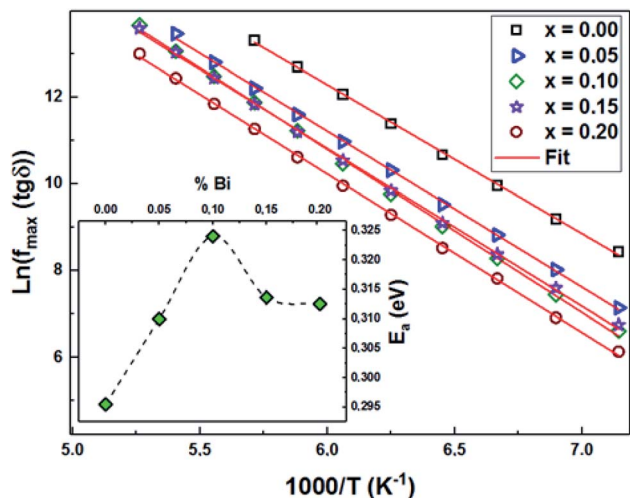
Fig. 15 Variation of ln(f_{max} (tan δ)) as a function of 1000/T and the activation energies corresponding to gains of (La$_{0.8}$Ca$_{0.2}$)$_{1-x}$Bi$_x$FeO$_3$ (x = 0.00, 0.05, 0.10, 0.15 and 0.20) compounds.

Fig. 17 The activation energies of (La$_{0.8}$Ca$_{0.2}$)$_{1-x}$Bi$_x$FeO$_3$ (x = 0.00, 0.05, 0.10, 0.15 and 0.20) compounds.

compounds, is shown in Fig. 16. From this figure, we can see that the alternative conductivity is characterized by two different regions suggesting that electrical conduction occurs *via* two different processes.

In the region of low temperatures (R1: T < 222 K), the conductivity is dependent on both frequency and temperature while for high temperatures (R2: $T \geq$ 222 K), it only depends on the temperature and shows a linear variation. The conduction
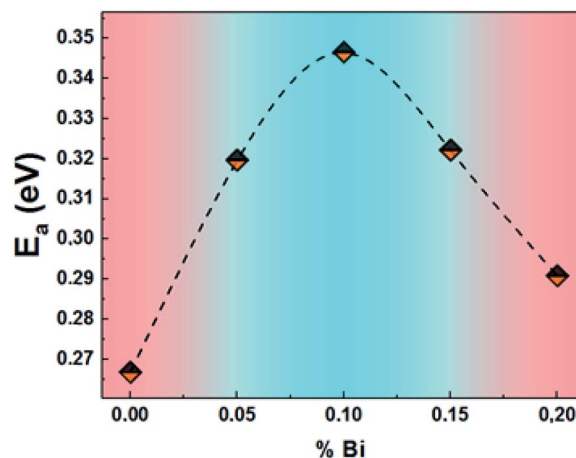
process in the first region will be studied in detail in the following, based on the thermal variation of the exponent "s" of Joncher's law. In the second region, we have calculated the activation energies of the alternative conductivity using Arrhenius' law:[53]

$$\sigma_{ac} \times T = \sigma_0 \exp\left(-\frac{E_a}{k_B T}\right) \quad (8)$$

The calculated activation energy values, from the slopes of each linear adjustment, are shown in Fig. 17. These values are in
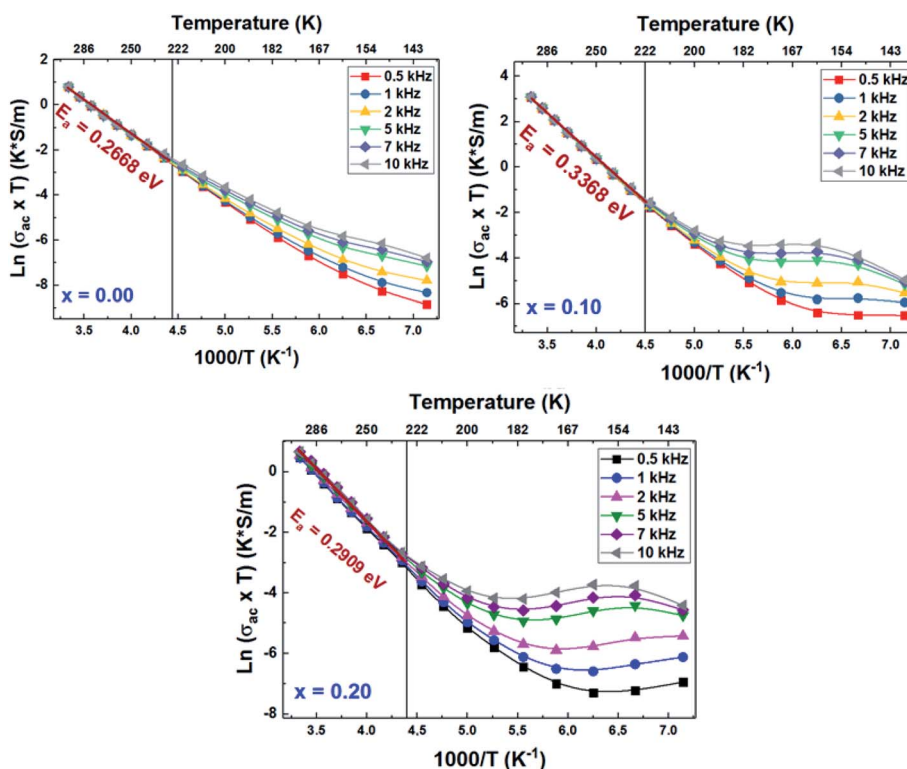

Fig. 16 Variation of ln($\sigma_{ac} \times T$) as a function of 1000/T of (La$_{0.8}$Ca$_{0.2}$)$_{1-x}$Bi$_x$FeO$_3$ (x = 0.00, 0.10 and 0.20) compounds.
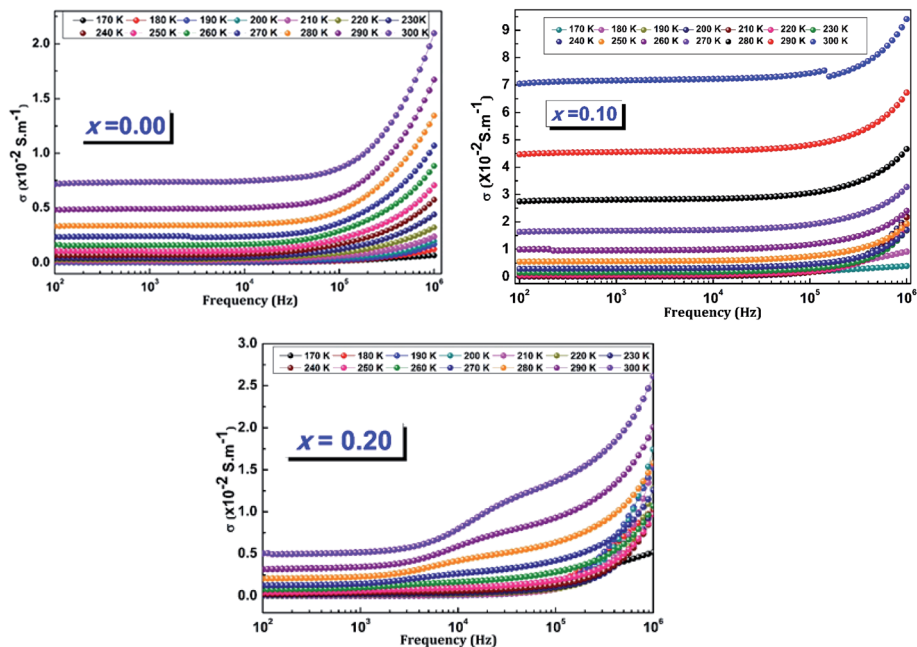
Fig. 18 Variation of the ac-conductivity (σ_{ac}) as a function of frequency at different temperatures of $(La_{0.8}Ca_{0.2})_{1-x}Bi_xFeO_3$ (x = 0.00, 0.10 and 0.20) compounds.

good agreement with those deduced previously, which suggests that the relaxation process and the electrical conductivity are attributed to the same type of charge carriers, namely the jump of electrons between the states of iron (Fe^{3+} and Fe^{4+}).

The frequency variation of the alternating conductivity for different temperatures of LCBFO compounds is shown in Fig. 18, which shows that the alternating conductivity is almost constant at low frequencies and increases with increasing temperature. This behaviour corresponds to the dc conductivity and confirms the decrease in resistance when the temperature increases. In high frequency regions, the alternating conductivity becomes frequency dependent.

The ac conductivity curves have been adjusted according to a power law known as Joncher:

$$\sigma_{ac}(\omega, T) = \sigma_{dc} + A \times \omega^{s(T)} \tag{9}$$

where, σ_{ac} is the conductivity at low frequencies (static) which depends on the temperature and $0 < s < 1$ represents the degree of interaction between the mobile ions with the environments which surround them. The results of adjustment of the conductivity (ac) using (eqn (9)), are collated in Table 7.

As described before, the "s" parameter of Jonscher's law is of great interest since its thermal variation allows us to identify the conduction process among the four known models.[54]

The variation of the exponent "s" as a function of the temperature for the LCBFO compounds is shown in Fig. 19.

We notice that "s" increases with increasing temperature. Thus, the NSPT model (small polaron tunnel conduction model) seems to be the most suitable to explain the conduction mechanism in the sol–gel compounds studied.

Table 7 Nonlinear fitting data of the conductivity of $(La_{0.8}Ca_{0.2})_{1-x}Bi_xFeO_3$ (x = 0.00, 0.05, 0.10, 0.15 and 0.20)

| T (K)	σ_{dc} ($\times 10^{-5}$ S m^{-1})	A ($\times 10^{-7}$)	S
x = 0.00			
140	0.45	2.34	0.23
150	0.63	1.78	0.31
160	0.02	1.96	0.36
170	0.05	1.24	0.47
180	0.12	1.75	0.57
190	0.4	9.46	0.63
200	0.72	4.38	0.72
210	0.11	2.698	0.82
220	2.04	2.99	0.91
x = 0.10			
140	5.87	2.87	0.34
150	7.93	5.87	0.40
160	4.97	1.74	0.46
170	3.31	2.23	0.53
180	50.5	3.65	0.61
190	87.3	4.75	0.75
200	136.4	1.44	0.92
210	202.7	1.17	0.94
220	287.2	6.16	1.00
x = 0.20			
140	0.03	5.76	0.30
150	0.08	2.56	0.46
160	0.09	3.24	0.59
170	0.07	4.25	0.68
180	0.22	3.51	0.76
190	0.63	1.67	0.83
200	2.23	7.33	0.87
210	8.57	1.26	0.91
220	16.60	1.19	0.94
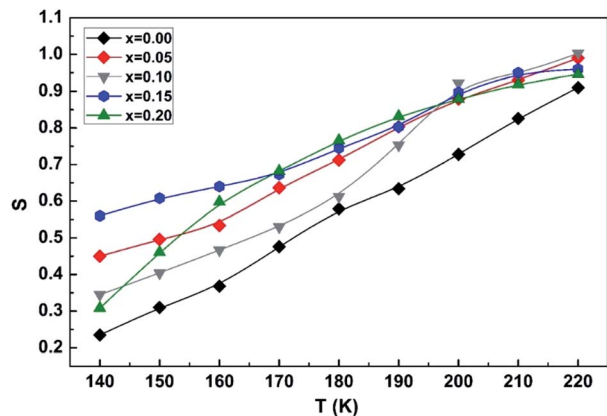
Fig. 19 Variation of the s exponent as a function of temperature of $(La_{0.8}Ca_{0.2})_{1-x}Bi_xFeO_3$ ($x = 0.00$, 0.05, 0.10, 0.15 and 0.20) compounds.

6 Conclusion

The present work has reported the results of the electrical and dielectric studies of $(La_{0.8}Ca_{0.2})_{1-x}Bi_xFeO_3$ ($x = 0.00$, 0.05, 0.10, 0.15 and 0.20) (LCBFO) compounds synthesized using a sol–gel method and annealed at $T = 800\ °C$. The electrical properties of our compounds have shown a strong dependence on temperature and frequency. The frequency dispersion of the real and imaginary components of the complex impedance enable to deduct that the insertion of Bi significantly decreases the resistance, complex impedance diagrams have revealed the presence of arcs not centered on the real axis, suggesting that the conduction of these materials follows the Cole–Cole model. The modeling of Nyquist diagrams, at different temperatures, allowed us to go back to the equivalent electrical circuit describing the behaviour of these compounds. The proposed equivalent electrical circuit is the series association of two circuits $[(R_{GB}//CPE_{GB})$ with $(R_G//C_G)]$. The study of the ac conductivity highlighted the existence of a mechanism by jump of the charge carriers between two successive sites, and showed that the insertion of Bi promotes the improvement of conductivity. Likewise, this study showed that the activation energy (E_a) values coincide with those deduced from the analysis of the spectra of the impedance, which allowed us to conclude that the electrical conduction and the phenomenon of relaxation can be attributed to the same type of charge carriers.

Conflicts of interest

There are no conflicts to declare.

Acknowledgements

References

1 S. Megahed and W. Ebner, *J. Power Sources*, 1995, **54**, 155.
2 M. Sugimoto, *J. Am. Ceram. Soc.*, 1999, **82**, 269.
3 M. Viret, D. Rubi, D. Colson, D. Lebeugle, A. Forget, P. Bonville and G. Dhalenne, *Mater. Res. Bull.*, 2012, **47**, 2294.
4 J. Suntivich, H. A. Gasteiger, N. Yabuuchi, H. Nakanishi, J. B. Goodenough and S. H. Yang, *Nat. Chem.*, 2011, **3**, 546.
5 B. C. Steele and A. Heinzel, *Mater. Sustainable Energy*, 2011, 224.
6 I. Sosnowska, T. P. Neumaier and E. Steichele, *J. Phys. C: Solid State Phys.*, 1982, **15**, 4835.
7 K. Huang, H. Y. Lee and J. B. Goodenough, *J. Electrochem. Soc.*, 1999, **145**, 3220.
8 M. H. Hung, M. V. M. Rao and D. S. Tsai, *Mater. Chem. Phys.*, 2007, **101**, 297.
9 A. Delmastro, D. Mazza, S. Ronchetti, M. Vallino, R. Spinicci, P. Brovetto and M. Salis, *Mater. Sci. Eng., B*, 2001, **79**, 140.
10 N. N. Toan, S. Saukko and V. Lantto, *Phys. B*, 2003, **327**, 279.
11 V. Lantto, S. Saukko, N. N. Toan, L. F. Reyes and C. G. Granqvist, *J. Electroceram.*, 2004, **13**, 721.
12 D. Wang and M. Gong, *J. Appl. Phys.*, 2011, **109**, 114.
13 S. Phokha, S. Pinitsoontorn, S. Rijirawat and S. Maensiri, *J. Nanosci. Nanotechnol.*, 2015, **15**, 9171.
14 V. V. Kharton, A. P. Viskup, E. N. Naumovich and V. N. Tikhonovich, *Mater. Res. Bull.*, 1999, **34**, 1311.
15 J. E. ten Elshof, M. H. R. Lankhorst and H. J. M. Bouwmeester, *J. Electrochem. Soc.*, 1997, **144**, 1060.
16 S. Komornicki, L. Fournes, J. Grenier, F. Menil, M. Pouchard and P. Hagenmuller, *Mater. Res. Bull.*, 1981, **16**, 967.
17 M. Vallet-Regí, J. González-Calbet, M. A. Alario-Franco, J.-C. Grenier and P. Hagenmuller, *J. Solid State Chem.*, 1984, **55**, 251–261.
18 E. K. Abdel-Khalek and H. M. Mohamed, *Hyperfine Interact.*, 2013, **222**(1), 57.
19 P. Ciambelli, S. Cimino, L. Lisi, M. Faticanti, G. Minelli, I. Pettiti and P. Porta, *Appl. Catal., B*, 2001, **33**, 193.
20 L. B. Kong and Y. S. Sheng, *Sens. Actuators, B*, 1996, **30**, 217.
21 A. Benali, M. Bejar, E. Dhahri, M. Sajieddine, M. P. F. Graça and M. A. Valente, *Mater. Chem. Phys.*, 2015, **149**, 467.
22 H. Saoudi, A. Benali, M. Bejar and E. Dhahri, *J. Alloys Compd.*, 2017, **731**, 655–661.
23 G. Pecchi, M. G. Jiliberto, A. Buljan and E. J. Delgado, *Solid State Ionics*, 2011, **187**, 27.
24 S. Smiy, H. Saoudi, A. Benali, M. Bejar and E. Dhahri, *Chem. Phys. Lett.*, 2019, **735**, 136765.
25 A. Benali, M. Bejar, E. Dhahri, M. F. P. Graça and L. C. Costa, *J. Alloys Compd.*, 2015, **653**, 506.
26 A. Benali, A. Souissi, M. Bejar, E. Dhahri, M. F. P. Graca and M. A. Valente, *Chem. Phys. Lett.*, 2015, **637**, 7.
27 H. Issaoui, A. Benali, M. Bejar, E. Dhahri, M. P. F. Graca, M. A. Valente and B. F. O. Costa, *Chem. Phys. Lett.*, 2019, **731**, 136588.
28 H. Issaoui, A. Benali, M. Bejar, E. Dhahri and B. F. O. Costa, *Hyperfine Interact.*, 2020, **241**, 26.

29 H. Issaoui, A. Benali, M. Bejar, E. Dhahri, R. F. Santos, N. Kus, B. A. Nogueira, R. Fausto and B. F. O. Costa, *J. Supercond. Novel Magn.*, 2018, **32**(6), 1571–1582.

30 R. Hamdi, A. Tozri, E. Dhahri and L. Bessais, *Intermetallics*, 2017, **89**, 118–122.

31 R. A. Young, *The Rietveld Method*, Oxford University Press, New York, 1993.

32 V. Goldschmidt, *Geochemistry*, Oxford University Press, 1958.

33 Y. Tokura and Y. Tomioka, *J. Magn. Magn. Mater.*, 1999, **200**, 1.

34 A. Guinier, in *Théorie et Technique de la radiocristallographie*, ed. X. Dunod, 3rd edn, 1964, p. 462.

35 P. Goel and K. L. Yadav, *J. Mater. Sci.*, 2007, **42**(11), 3928.

36 F. Bordi, C. Cametti and R. H. Colby, *J. Phys.: Condens. Matter*, 2004, **16**, 1423.

37 N. Rezlescu, P. D. Popa, E. Rezlescu and C. Doroftei, *J. Phys.*, 2008, **53**, 545.

38 Q. Rong, Y. Zhang, T. Lv, K. Shen, B. Zi, Z. Zhu and Q. Liu, *Nanotechnology*, 2018, **29**(14), 145503.

39 A. Bougoffa, J. Massoudi, M. Smari, E. Dhahri and K. Khirouni, *J. Mater. Sci.: Mater. Electron.*, 2019, **30**(24), 21031.

40 B. Bechera, P. Nayak and R. N. P. Choudhary, *Mater. Res. Bull.*, 2008, **43**, 401.

41 M. Haibado, B. Louati, F. Hlel and K. Guidara, *J. Alloys Compd.*, 2011, **509**, 6083.

42 D. Bouokkeze, J. Massoudi, W. Hzez, M. Smari, A. Bougoffa and K. Khirouni, *RSC Adv.*, 2019, **9**(70), 40940.

43 A. Kumar, B. P. Singh, R. N. P. Choudhary and A. K. Thakur, *Mater. Chem. Phys.*, 2006, **99**, 150.

44 K. K. Srivastava, A. Kumar, O. S. Panwar and L. N. Lakshminarayan, *J. Non-Cryst. Solids*, 1979, **3**, 33.

45 M. Shivanand, B. Ponraj, R. Bhimireddi and K. B. R. Varma, *J. Am. Ceram. Soc.*, 2017, **100**, 2641.

46 V. G. Nair, A. Das, V. Subramanian and P. N. Santhosh, *J. Appl. Phys.*, 2013, **113**, 213907.

47 R. Ertugrul and A. Tataroglu, *Chem. Phys. Lett.*, 2012, **29**, 077304.

48 P. B. Macedo, C. T. Moynihan and R. Bose, *Phys. Chem. Glasses*, 1972, **13**(6), 171.

49 A. Shukla, R. N. P. Choudhary and A. K. Thakur, *J. Phys. Chem. Solids*, 2009, **70**(11), 1401.

50 A. Kumar, P. Kumari, A. Das, G. D. Dwivedi, P. Shahi, K. K. Shukla, A. K. Ghosh, A. K. Nigam, K. K. Chattopadhyay and S. Chatterjee, *J. Solid State Chem.*, 2013, **208**, 120.

51 S. Hcini, A. Selmi, H. Rahmouni, A. Omri and M. L. Bouazizi, *Ceram. Int.*, 2017, **43**(2), 2529.

52 C. T. Moynihan, *Solid State Ionics*, 1998, **105**, 175.

53 M. Ganguli, M. Harish Bhat and K. J. Rao, *Phys. Chem. Glasses*, 1999, **40**(6), 297.

54 R. L. Frost, P. A. Williams, J. T. Kloprogge and P. Leverett, *Raman Spectrosc.*, 2011, **32**, 906.